PHYSICAL REVIEW B **109**, 024440 (2024)

Dynamic electromagnonic crystals based on ferrite-ferroelectric thin film multilayers

Aleksei A. Nikitin ,[1,*] Nikolai Kuznetsov ,[2] Sebastiaan van Dijken ,[2] and Erkki Lähderanta [1]
[1]*Department of Physics, LUT University, 53850 Lappeenranta, Finland*
[2]*NanoSpin, Department of Applied Physics, Aalto University School of Science, P.O. Box 15100, FI-00076 Aalto, Finland*

(Received 5 October 2023; revised 27 November 2023; accepted 10 January 2024; published 30 January 2024)

Magnons, the quanta of the oscillations of localized electron spins, are a powerful tool for information transport and processing of microwave signals. Owing to the challenge of energy efficient spin-wave control on small time- and space scales, dynamic magnonic crystals have been proposed. Their distinct feature is the possibility to toggle on and off the spatial periodicity of the magnetic waveguide that allows one to realize the unusual signal processing functions. The miniaturization of magnonic circuits, reduction in energy consumption, and fast operation are important possibilities of these artificial crystals. These can be achieved in ferrite-ferroelectric (multiferroic) heterostructures, where strong coupling of magnons and microwave photons constitutes quasiparticles called electromagnons. Using both a theoretical approach and microwave measurements, we report on successful dynamic control of electromagnonic band structures in artificial thin film crystals via application of a voltage to the grid electrode located on a ferroelectric film. A promising functionality of the proposed waveguiding structures arises from two major factors: (i) low energy consumptions due to the thin ferroelectric layer, and (ii) pronounced rejection bands caused by a gradual change of the dielectric permittivity.

DOI: 10.1103/PhysRevB.109.024440

I. INTRODUCTION

Information can be transferred in diverse magnetic materials, including insulators, in the form of a spin wave [1–3]. Investigations of a wide variety of linear [4–6] and nonlinear [7–9] spin-wave phenomena address the field of science known as magnonics. The promising building blocks for magnonic devices are constituted by artificial spatially periodic magnetic media, known as magnonic crystals [10–17]. Their functionality arises from a band structure engineering that is mainly caused by spin-wave Bragg reflections from periodic disturbances. However, these crystals have static properties, which are predefined by the fabrication and cannot be modified later. Time-dependent control of the waveguiding properties resolves the above-mentioned restriction and makes it possible to toggle on and off the spatial periodicity of the magnetic waveguide, known as the dynamic magnonic crystal (DMC) [18–22]. Most DMCs are controlled by an electric current in metal wires or in periodic screens leading to generation of waste heat. A more challenging, but more energy-efficient approach is to utilize the electric field controlled crystals [23–26].

Voltage control of magnon currents representing a form of spin currents [27] promises to be fast and low energy consuming. This can be achieved in ferrite-ferroelectric (multiferroic) heterostructures, where an electrodynamic interaction between high-frequency electromagnetic and spin waves leads to the formation of hybrid spin-electromagnetic waves (SEWs) [28]. Dispersion characteristics of SEW combine features of electromagnetic waves in ferroelectric-based materials and spin waves in ferrites. Therefore, the resulting wave spectrum is dually controllable by both electric and magnetic fields. The electric tuning is realized through a variation of the dielectric permittivity of a ferroelectric layer by changing an applied electric field, while the magnetic tuning is provided by a dependence of the magnetic permeability of ferrites on a bias magnetic field. The SEW quanta are considered electroactive magnons or electromagnons. By analogy to the known magnonic and photonic crystals, the multiferroic periodic heterostructures, called electromagnonic crystals, demonstrate band gaps in SEW spectra [29,30]. A working dynamic electromagnonic crystal (DEMC) based on artificial multiferroic heterostructures was experimentally demonstrated recently [31]. Although the presented crystal has relatively large dimensions and requires an application of the large voltage of 1800 V, it is more efficient than the other proposed methods of dynamic control of the spin-wave band structure [18,19] since the electrical power is required only when switching the electric field on/off.

A miniaturization of a ferroelectric layer opens up further opportunities for advanced DEMC with low energy consumption. Namely, thin film multiferroics allows one to reduce the control voltage needed for well-pronounced electric field control of the wave propagation [32–34]. It has been recently shown that regular waveguides made of the ferrite-ferroelectric-ferrite three-layer structures enrich the properties of multiferroics because of a hybridization among one electromagnetic mode and two spin-wave modes in the closely spaced ferrite films [35–39]. In this case, SEW spectra are formed as the result of the two types of coupling: (i) electromagnetic interaction between spin and electromagnetic modes, and (ii) magnetodipole interaction between two spin waves modes. This feature allows one to increase the efficiency of electric field control of SEWs propagating in two ferrite films separated by a thin ferroelectric layer. Namely,

---

[*] aleksei.a.nikitin@gmail.com

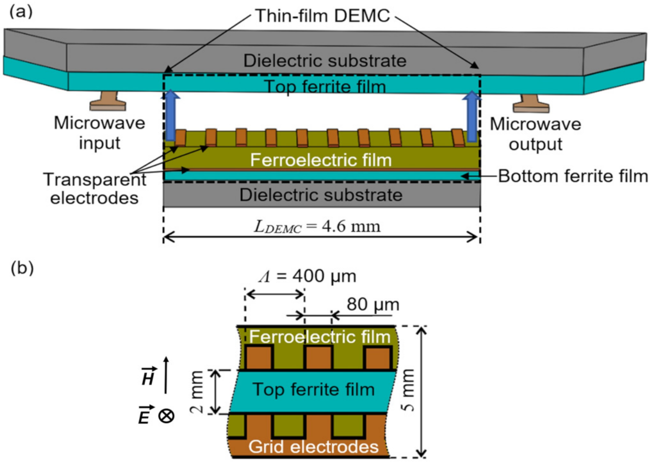

FIG. 1. (a) Thin film dynamic electromagnonic crystal (DEMC) based on ferrite-ferroelectric multilayer. It consists of ferroelectric layer with thickness $\delta = 25\,\mu$m and two (top and bottom) ferrite layers with thickness $t_1 = 13.6\,\mu$m and $t_2 = 5.5\,\mu$m, respectively. The grid electrode consists of ten stripes with thickness 100 nm and width 80 μm, which are placed on top of the ferroelectric film. (b) A top view of a fragment of the DEMC.

this control originated from the change of the magnetodipole interaction between the ferrite films by the variation of the dielectric permittivity of a ferroelectric layer. A decrease in the dielectric permittivity can be considered as a reduction in effective spatial distance between the magnetic films, leading to an increase in the coupling of spin-wave modes in the magnetic films. This topic has special potential considering recent theoretical and experimental progress that links the wave dynamics of thin film structures to the static electromagnonic band formation [40].

In this work, we present a realization of a thin film DEMC operating with electromagnons at microwave frequencies. In contrast to existing multiferroic waveguides, where spatial periodicity was realized by a change in the properties of the adjacent ferroelectric slab, our DEMC design allows one to combine thin film ferrite and ferroelectric elements for the tailoring of band structures in a single voltage-controlled device.

II. DESIGN OF THE DYNAMIC ELECTROMAGNONIC CRYSTAL

A schematic of the investigated structure is shown in Fig. 1(a). The DEMC consists of two ferrite films separated by a ferroelectric layer with zero voltage permittivity $\varepsilon(0) = 1490$. It comprises a grid electrode consisting of $N = 10$ stripes with a thickness of 100 nm and a width of 80 μm, which are patterned on top of the ferroelectric film [(see Fig. 1(b)]. During investigations, we stress that the grid electrode is transparent for a microwave field of waves propagating in the structure and does not introduce any disturbance in their propagation. It was confirmed by measurements of the transmission characteristics of the dynamic electromagnonic crystal. The period of the metal grid, Λ, is 400 μm. In simulations, the thickness of the ferroelectric film δ is varied from 15 to 75 μm, while the bias voltage U applied to the grid electrodes is changed from 0 to 120 V. The top and bottom ferrites have thickness $t_1 = 13.6\,\mu$m and $t_2 = 5.5\,\mu$m, respectively, as well as saturation magnetization $M_1 = 143.24$ kA/m and $M_2 = 153.58$ kA/m at room temperature. The ferromagnetic resonance linewidth ΔH of the ferrite layers is assumed to be constant with frequency. In accordance with Fig. 1, the DEMC itself is a part of the top ferrite film waveguide with a propagation path of $L_{\mathrm{DEMC}} = 4.6$ mm making contact to the ferrite-ferroelectric bilayer with the metal grid electrodes. The structure is magnetized by a uniform magnetic field of $H = 127.324$ kA/m applied along the grid electrodes to establish the condition for magnetostatic surface spin-wave excitation.

Some comments about the design of the DEMC should be added. Firstly, the proposed set of ferrite parameters ensures a strong magnetodipole interaction between spin-wave modes in the closely spaced ferrite films. The strength of this interaction is strongly dependent on the overlapping of the dynamic fields of spin-wave modes. The dynamic magnetic fields of the surface spin waves propagating in the lower and upper ferrite layers have weak exponential transverse distributions with the maxima lying at the upper surfaces of both layers. This means that the overlapping depends on the geometry of the layered structures and parameters of the materials. In the case of identical micron-sized ferrite films, the spin-wave modes demonstrate a strong coupling for relatively small wave numbers (up to 10 rad/cm). An increase in the wave numbers leads to a decrease in the interaction. This is explained by the dependence of the damping decrements of the alternating fields outside the ferrite films on the wave number. Therefore, waves having relatively large wave numbers propagate independently and their dispersion branches tend to follow the dispersion of the separate ferrite films. To realize a pronounced rejection band in the proposed dynamic electromagnonic crystal, an effective magnetodipole interaction should be realized in a broad range of wave numbers, where the band structure is formed. As follows from the conventional Bragg analysis, an interaction of waves in the proposed DEMC leads to the formation of the rejection bands at wave numbers $K_{Bn} = n\pi/\Lambda$, where n is a band-gap number. Namely, the first three rejection bands should be formed at 78.54, 157, and 235.6 rad/cm, respectively. This means that nonidentical ferrite layers, where a broad range spin-wave coupling is realized, should be used. In this case, the strength of spin-wave interactions is determined by a phase velocity contrast, which is affected by a ratio of the thicknesses and the saturation magnetization of the ferrite layers. Some possible cases are summarized in Fig. 2. To achieve a strong interaction between surface spin-wave modes, an effective overlapping of their dynamic components of the magnetic fields should be realized. It can be achieved when the configuration of two ferrite films fulfills the condition shown in Fig. 2(d). Here, the dispersion branches for thin and thick ferrite layers shown by solid green and dashed blue curves, respectively, cross each other in the magnetostatic region. In this case, the overlapping of the dynamic fields of spin-wave modes is increased in comparison with other configurations [see Figs. 2(a)–2(c)], which leads to enhancement of the magnetodipole interaction between nonidentical ferrite films.

Secondly, robust operation of the proposed DEMC depends on the effectiveness of spin-wave excitation and reception.

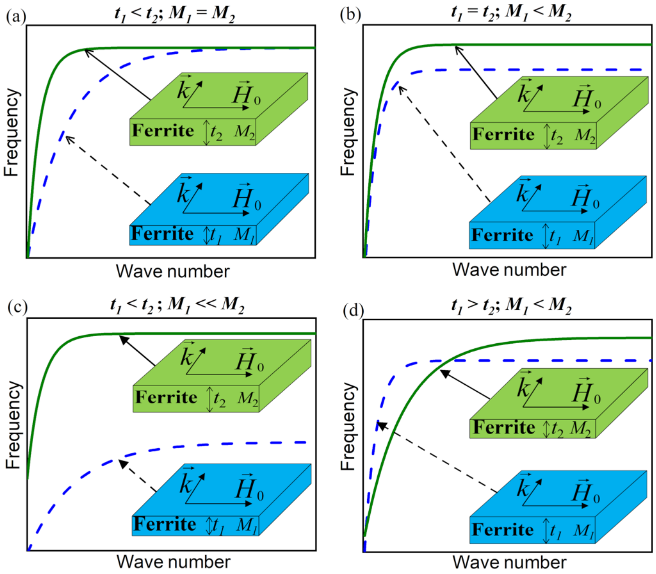

FIG. 2. Qualitative pictures of spin-wave dispersion characteristics of uncoupled ferrite films with various thicknesses (t_1, t_2) and saturation magnetizations (M_1, M_2). The dependencies are shown inside the magnetostatic region with wave numbers less than 10^4 rad/cm. In the calculations, the following thickness and saturation magnetization values were used: (a) $t_1 = 6\,\mu\text{m}$, $t_2 = 20\,\mu\text{m}$, $M_1 = M_2 = 139.26$ kA/m; (b) $t_1 = t_2 = 20\,\mu\text{m}$, $M_1 = 139.26$ kA/m, $M_2 = 142.44$ kA/m; (c) $t_1 = 6\,\mu\text{m}$, $t_2 = 20\,\mu\text{m}$, $M_1 = 119.37$ kA/m, $M_2 = 139.26$ kA/m; (d) $t_1 = 20\,\mu\text{m}$, $t_2 = 6\,\mu\text{m}$, $M_1 = 139.26$ kA/m, $M_2 = 142.44$ kA/m.

To accomplish this, we used a standard microstrip structure [41], where short-circuited microstrip antennas are positioned on the surface of the top ferrite film [see Fig. 1(a)]. This provides the opportunity to convert surface spin waves into SEWs through an effective overlapping of the dynamic components of the magnetic fields of spin-wave modes coupled by strong magnetodipole interactions and electromagnetic wave mode TE_1 localized mostly in the ferroelectric layer.

Finally, the application of a control voltage U to the grid electrodes provides a reliable approach to create periodically modulated properties in the proposed structure. For the considered configuration, the electric field induces a spatial modulation of the dielectric permittivity ε. To simulate this effect, we solved the two-dimensional Poisson equation taking into account both the geometry of the grid electrodes and the dependence $\varepsilon(U)$, as detailed in Appendix A. In the calculations, barium-strontium titanate $[Ba_{0.5}Sr_{0.5}TiO_3(BST)]$ was chosen as the ferroelectric owing to its low dielectric loss and strong dependence $\varepsilon(U)$. Figure 3(a) shows the calculated distribution of the dielectric permittivity for a 25 μm thick ferroelectric film under an applied voltage of 120 V. This figure is plotted on a linear color scale, where high ε is indicated as blue and low ε as red.

III. NUMERICAL MODELING AND UNDERLYING PHYSICS

To investigate the band structure, the wave dynamics in the DEMC was modeled numerically and later verified experimentally. Theoretical transmission characteristics were calculated by means of a two-step algorithm. As a first step, the complex dispersion relation $\omega^*(k) = \omega(k) + j\omega_r(k)$ for each region of the layered structure with constant dielectric permittivity ε_i was found using the theory presented in [32]. This is an important step because dispersion characteristics are uniquely related to the waveguiding transfer functions.

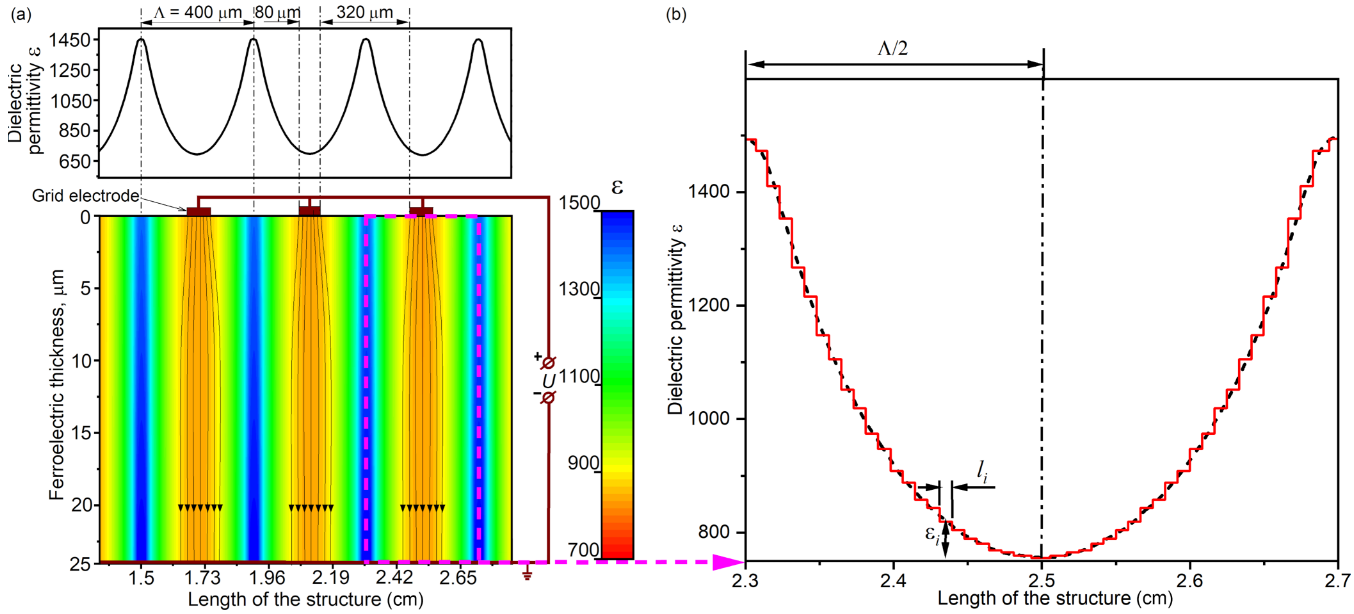

FIG. 3. (a) Spatial distribution of the dielectric permittivity ε after application of electrical voltage $U = 120$ V to the grid electrode located on the top of the 25 μm thick ferroelectric film. (b) Calculated spatial distribution of the dielectric permittivity after application of 120 V to the grid electrode within one period of the DEMC. Here, the dashed black line represents the dependence calculated by the two-dimensional Poisson equation, while the solid red line shows the fitting curve consisting of 48 regions.

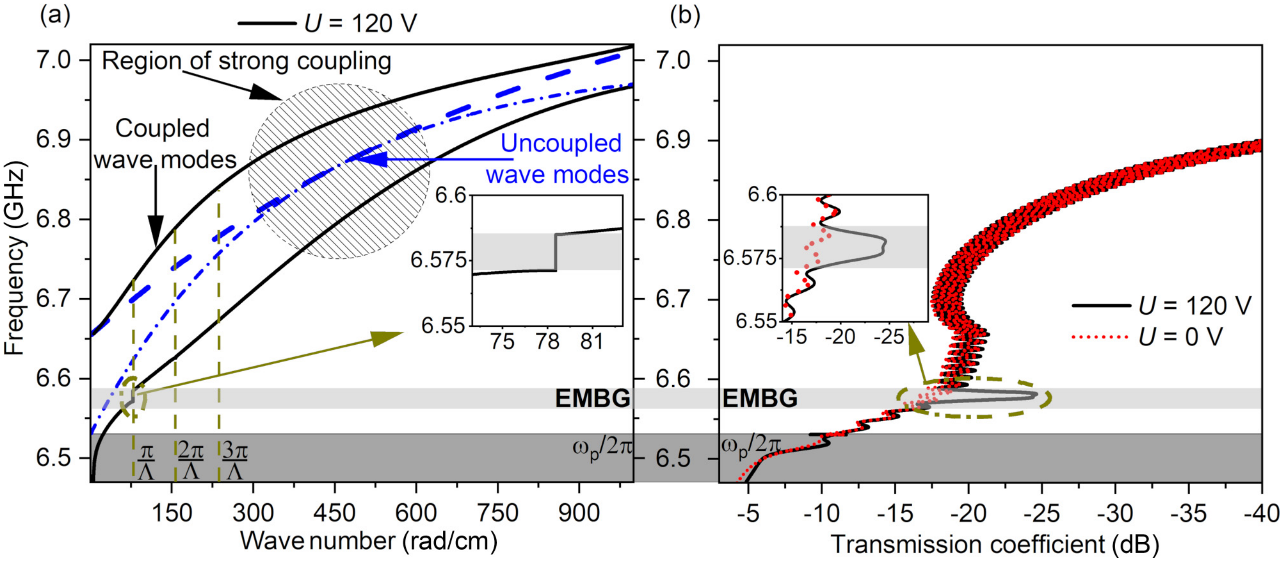

FIG. 4. (a) Dispersion characteristic of spin-electromagnetic waves for an applied voltage $U = 120$ V (see solid black line). The dashed and dash-dotted blue curves show dispersion characteristics of surface spin waves determining the lower cutoff frequency $\omega_p/2\pi$. The dark gray area below this frequency indicates an impossibility to excite waves in the proposed design of the DEMC. The inset shows a fragment of the dispersion characteristic near the first electromagnonic band gap (EMBG) marked by light gray color. (b) Transmission characteristics of the DEMC for zero voltage (dashed red curve) and for $U = 120$ V (solid black curve).

The real part of the dispersion relation $\omega_{\mathrm{r}}(k)$ defines a group velocity of waves and its imaginary part $\omega_r(k)$ describes the propagation loss. The combination of these quantities allows one to calculate transmission characteristics of each region of the layered structure. As a second step, the resulting transmission characteristic of the DEMC was obtained using a transfer-matrix method [42] allowing one to realize an effect of a set of the regions by cascading them. This method allows one to calculate transmission characteristics of waveguiding structures with periodically modulated properties in the shape of rectangles with the same thickness and width. In YIG-based magnonic crystals, the transfer-matrix method is applicable because their regions with constant properties are produced by periodic variations of the thickness [43], width [44], magnetization [45,46], and metallization [47]. In these cases, the rectangular cross section of the periodic disturbances is predetermined. The proposed DEMC differs conceptually from these magnetic media because it lacks abrupt borders between periodic disturbances. As seen from Fig. 3(a), the value ε varies gradually induced by an electrical voltage. To apply the transfer-matrix method for the considered structure, we divided one period of the DEMC into $P = 48$ regions with length l_i consisting of two ferrite films and a ferroelectric layer with dielectric permittivity ε_i, where i is any integer from 1 to P. This allows one to describe the distribution of ε by the step function as shown in Fig. 3(b). Note that a further increase in the number of regions P changes the result of the numerical calculation by less than 1% but provides a sufficient increase in the calculation time. Table I, which contains information about the dielectric permittivity ε_i of the ferroelectric layer and its length l_i within one period of the DEMC, is given in Appendix B.

To solve this electrodynamic problem, the standard transfer-matrix method was modified to describe the propagation and reflections of waves in each region within one period of the DEMC, as discussed in Appendix C. Results of the numerical modeling are shown in Fig. 4. The black solid curves in Fig. 4(a) show the calculated dispersion characteristics in the DEMC after applying a voltage $U = 120$ V, while blue lines represent, for comparison, uncoupled spin-wave dispersion characteristics in the top (see dash-dotted line) and bottom (see dashed line) ferrite films. The obtained results show that a strong coupling between spin-wave modes takes place around the point of crossing their pure modes marked in Fig. 4(a). The sign of strong coupling is the large curvature of the SEW dispersion branches. More details about the principle of the hybrid wave formation in ferrite-ferroelectric thin film multilayers are presented in Appendix D. For the considered structure, the strength of spin-wave interaction depends mostly on three factors: (i) a ratio of the thicknesses and the saturation magnetization of the ferrite films; (ii) a distance between the ferrite films, i.e., a thickness of the intermediate ferroelectric layer; and (iii) a value of a dielectric permittivity of the ferroelectric layer. A variation of one of these parameters changes a coupling strength between spin-wave modes resulting in stronger/weaker repulsion of the dispersion branches around the point of the intersection of the uncoupled spin-wave modes. This behavior corresponds with the experimental and theoretical results presented in previous reports [48–51].

One can see from Fig. 4(a) that an area of strong coupling between spin-wave modes is realized outside the region where the band structure is formed. The position of this area is caused by two reasons. Firstly, magnetodipole interaction should be strong enough to realize pronounced rejection bands in DEMCs. It means that the spin-wave modes should be coupled in a broad range of wave numbers from 70 to 300 rad/cm, where DEMC band structure is formed. Secondly, in experiments the used method of wave excitation would not allow for observations below the spin-wave cutoff frequency $\omega_p/2\pi = 6.53$ GHz (see area of dark gray color in Fig. 4). Therefore, magnetodipole interaction should not be too strong inside wave number range 70–300 rad/cm to avoid the formation of the first rejection band below this cutoff frequency. This is because of the interaction between wave modes manifesting itself in a strong repulsion of the dispersion branches around the point of the intersection of uncoupled spin-wave modes. As seen from Fig. 4(a), the repulsion becomes less pronounced for smaller wave numbers.

The detailed analysis of the dispersion characteristics presented in Fig. 4(a) shows that the first electromagnonic band gap (EMBG) formed at the Bragg wave vector $k_B = \pi/\Lambda$ is much broader than those of high-order bands. As a result, only one pronounced rejection band marked by the light gray color is observed in the transmission characteristic shown in Fig. 4(b). The physical mechanism underlying the appearance of the EMBG can be understood as follows. Initially, the multiferroic heterostructure without application of a voltage represents a spatially homogeneous waveguide for SEWs. Due to this fact, the transmission characteristic of the structure exhibits slowly increasing losses [see dotted red line in Fig. 4(b)]. As a result, the electromagnon currents flow through the DEMC without backscattering resulting in the transmission characteristic as in a regular waveguide. In addition, one can see some oscillations in Fig. 4(b). In an experiment, one can observe this behavior which is basically caused by an interference of fundamental modes in each ferrite film. To take it into account during theoretical modeling, the constituting characteristics were found separately for the waves propagating as fundamental modes for each ferrite film. The resulting transmission characteristic was calculated as a superposition of the two interfering waves.

The application of a voltage to the grid electrodes causes a local reduction of ε across the ferroelectric film [see Fig. 3]. This produces a periodic array of reflectors, where the group velocity of the electromagnetic mode is varied. Under these conditions, excited waves undergo the cumulative effect of scattering, resulting in the formation of spectral regions with prohibited propagation. For the proposed DEMC configuration, the application of a bias voltage of 120 V produces a first rejection band in the vicinity of 6.576 GHz, where the dip in the transmission characteristic is formed. Removal of the bias voltage transforms the DEMC back to a spatially homogeneous multiferroic waveguide.

The shape and width of the EMBG depend on several parameters, such as the thickness δ of the ferroelectric film and the value of the external electric field $E = U/\delta$. The influence of these parameters on the band structure is shown in Fig. 5. Here the black solid lines are identical to the spectrum shown in Fig. 4(b).

As shown in Fig. 5(a), an increase of the ferroelectric film thickness leads to a frequency shift and broadening of the rejection band. This behavior is caused by a change in the difference between the SEW group velocity in the DEMC segments with spatially modulated dielectric permittivity. At the same time, thinner ferroelectric films produce higher loss of the microwave signal within the pass bands, resulting in a less pronounced rejection band.

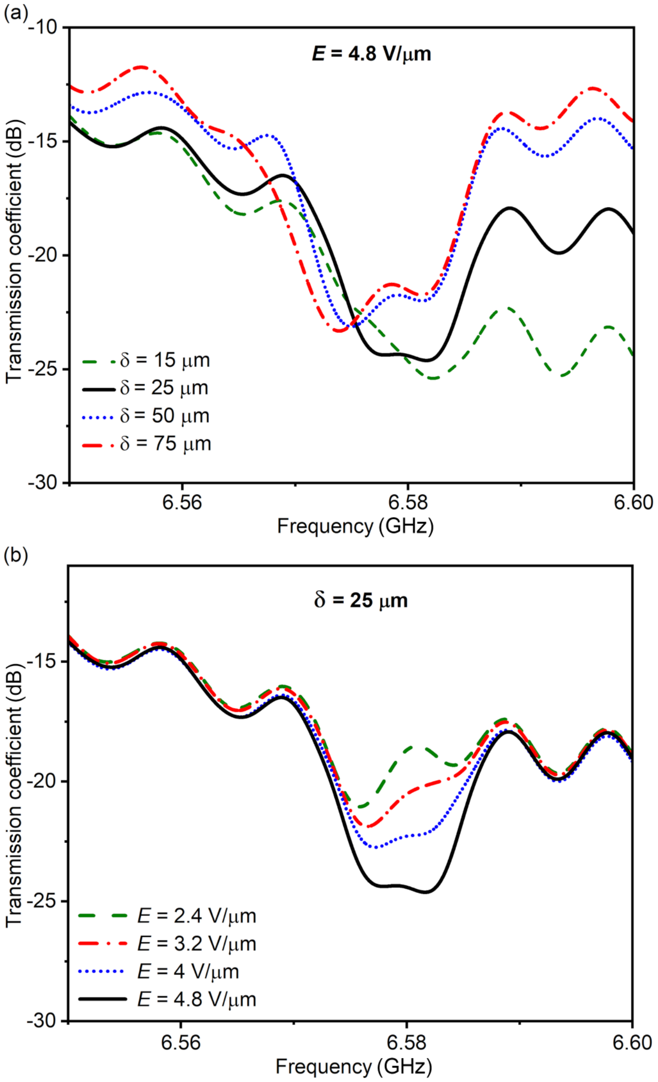

FIG. 5. Fragments of the transmission characteristics around the first rejection band for (a) different thickness δ of the ferroelectric film for fixed $E = 4.8$ V/μm and (b) different electric field E for fixed $\delta = 25$ μm.

Electric field control of the EMBG is shown in Fig. 5(b). The proposed DEMC with 25 μm thick ferroelectric film combines the advantages of a relatively low control voltage and a pronounced first rejection band. Therefore, we estimated the tuning ranges in the vicinity of this rejection band. The obtained results show that a rejection band depth in decibels increases by applying higher electric field E. This behavior is confirmed by the Bragg resonance condition, where the depth of a rejection band is mainly defined by the reflection efficiency of waves from an array of reflectors. For the proposed configuration of the DEMC, the reflection efficiency depends on the difference between dielectric permittivity of the periodically poled regions of the ferroelectric layer that becomes more pronounced with increasing electric field.

IV. EXPERIMENTAL TESTING

To check the adequacy of the developed theoretical model, we carried out experimental research using a ferrite-ferroelectric thin film multilayer as a measurement cell. The prototype of a DEMC was composed of two single-crystal yttrium iron garnet [$Y_3Fe_5O_{12}$(YIG)] films separated by a barium strontium titanate [$Ba_{0.5}Sr_{0.5}TiO_3$(BST)] layer having metal grid electrodes. Two ferrite films were fabricated from 13.6- and 5.5-μm YIG films grown by liquid-phase epitaxy on gadolinium gallium garnet [$Gd_3Ga_5O_{12}$(GGG)] substrates. The thick spin-wave waveguide was cut from the YIG/GGG wafer into a 3 cm long and 2 mm wide stripe with a saturation magnetization $M_1 = 143.24$ kA/m at room temperature, while the thin ferrite film had in-plane dimensions of $4 \times 2\ \text{mm}^2$ and $M_2 = 153.58$ kA/m.

The BST layer was fabricated by a conventional mixed oxide route followed by sintering in air. After that, a hydraulic press and subsequent annealing formed the BST slab. At room temperature, the produced slab had an isotropic dielectric permittivity of 2300 at 5 GHz confirming the paraelectric nature of the sample. The slab was polished down to a thickness of 100 μm and cut into stripes with in-plane dimensions of $4 \times 2\ \text{mm}^2$. This thickness is enough to demonstrate the validity of the obtained theoretical results. As shown in Fig. 5(a), an increase of the ferroelectric thickness leads to a small down-frequency shift and broadening of the rejection band.

To form the DEMC, a ten-stripe grid electrode made of 3-nm Ta/120-nm Au was patterned using optical lithography with a maskless aligner, *e*-beam evaporation, and lift-off. The stripe width was 110 μm and the grid period was 420 μm. The DEMC was positioned in a way that metal grid electrodes were in contact with the surface of the thin YIG film. To accomplish excitation and reception of waves, short-circuited microstrip antennas with a width of 50 μm and a length of 2.5 mm were used. The antennas were positioned at a distance of 7.3 mm. The structure was magnetized by a bias magnetic field $H = 127.324$ kA/m applied across the multiferroic structure along the antennas.

We measured DEMC transmission characteristics using a vector network analyzer R&S®ZVB-20. As expected from the theoretical calculations, the application of a voltage to the grid electrodes leads to the formation of a pronounced rejection band in transmission characteristics shown in Fig. 6(a). Here, the red dashed line represents the frequency response of the DEMC without applying a control voltage. In this case, the structure represents a spatially inhomogeneous medium for waves. The application of a voltage to the grid electrodes creates a spatially periodic electric field across the BST layer inducing a modulation of its dielectric permittivity. This results in formation of a rejection band as shown in Fig. 6(a) by the blue dash-dotted and black solid lines. For the performed experiment, the width of the deepest rejection band is about 9 MHz, and its depth is about 8 dB.

Although the presented transmission characteristic of the DEMC has relatively large insertion losses, our approach demonstrates a more pronounced band structure in comparison with the crystal based on a ferroelectric slab [31], where the width and depth of the deepest rejection band are about 1 MHz and 5 dB, respectively. At the same time, the minimum loss level of the proposed device remains comparable to that presented in [31]. Such a high value of the insertion loss is observed because of the large reflection of the incident microwave signal and additional reflections of the incident wave from the edges of the layered structure. One should recall that the YIG/BST bilayer covers only the central 4-mm length of the waveguiding ferrite film. Note that the insertion loss can be reduced significantly through matching the microstrip antenna with the feeding line, as well as through optimization of the geometry of the transition region from the YIG film to the multiferroic structure.

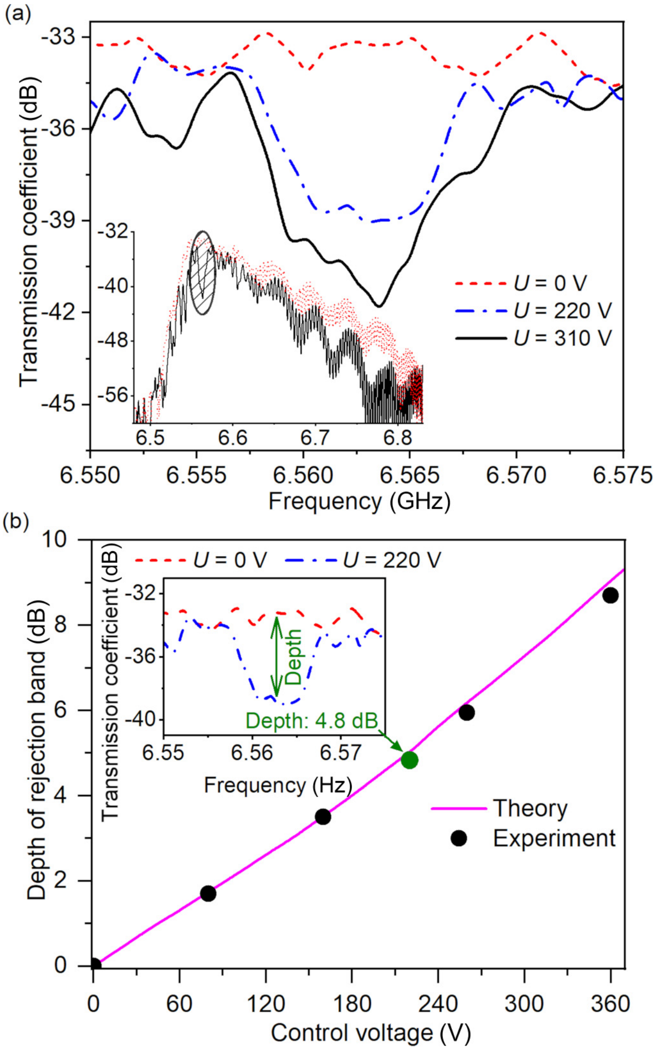

FIG. 6. (a) Fragment of the experimental transmission characteristics around the first rejection band of the DEMC measured for different control voltage *U*. (b) Dependence of the depth of the first rejection band versus the control voltage obtained from experimental data (black circles) and theoretical modeling (magenta solid line).

To compare experimental and theoretical data, we performed additional measurements to gauge the effect of an electric field on the DEMC band structure shown in Fig. 6(b). Here, the experimental values of the rejection band depth are presented by black circles, while the magenta solid line shows the theoretical dependence. Theoretical values were obtained as a difference of transmission coefficients for the DEMC in off and on states at a central frequency of a studied rejection band. Note that theoretical dependencies of transmission characteristics were calculated by the same algorithm described in Sec. III "Numerical modeling and underlying physics." As one can see, the theory is in good agreement with the experiment. The obtained results demonstrate that the rejection band depth in decibels varies almost linearly with the applied voltage. The deviation from a linear dependence is increased with the applied voltage. This behavior is caused mainly by a nonlinear dependence of dielectric permittivity ε on an applied control voltage U. At the same time, an increase of the rejection band depth is confirmed by the Bragg resonance condition, where the depth of a rejection band is mainly defined by the reflection efficiency of waves from an array of reflectors. In the considered case, this efficiency depends on the difference between dielectric permittivity of the periodically poled regions that becomes more pronounced with increasing electric field.

V. CONCLUSION

In summary, we have developed, numerically simulated, and experimentally demonstrated a dynamic electromagnonic crystal operating with low control voltage. It was shown that the proposed device differs conceptually from earlier investigated periodic structures because it lacks abrupt borders between periodic disturbances. To estimate the contribution of this effect to band-gap formation, we modified the transfer-matrix method. During the modeling, we found out that a gradual change of the dielectric permittivity provides an increase of the rejection efficiency due to an increase of wave reflections from induced disturbances. This results in more accurate predictions of the band structure of electromagnonic crystals containing ferroelectric layers. Namely, the application of the bias voltage of 120 V to the grid electrodes deposited on a 25 μm thick ferroelectric film produces a pronounced rejection band with a depth of almost 10 dB, which is comparable to current-controlled dynamic magnonic crystals [18]. Moreover, the formation of voltage-controlled rejection bands in the transmission characteristics of artificial crystal only requires an electric field of 4.8 V/μm. In contrast, electric field control of perpendicular magnetic anisotropy in reconfigurable magnonic crystals [23] and in logic devices [25] requires more than 100 V/μm. Thus the proposed structure has a good potential for applications as a complementary part to the traditional approach for general computing and microwave signal processing.

ACKNOWLEDGMENTS

This work was supported by the INERCOM platform of LUT University. We acknowledge the provision of facilities by Aalto University at the OtaNano-Micronova Nanofabrication Centre.

APPENDIX A: SIMULATION OF A DIELECTRIC PERMITTIVITY DISTRIBUTION ACROSS FERROELECTRICS

The spatial distribution of the electric field in the longitudinal section of the ferroelectric layer was calculated by using the finite element method in the original scripted environment FLEXPDE. It was assumed that the distribution of charges and fields inside the ferroelectric obey the two-dimensional Poisson equation $\nabla \cdot E = -\nabla^2 \varphi = \rho/[\varepsilon_0\, \varepsilon(U)]$, where E is an electric field, φ is an electric potential, ρ is a total volume charge density, and $\varepsilon_0 = 8.85 \times 10^{-12}$ F/m is vacuum permittivity. As seen, the Poisson equation additionally takes into account the dependence of the dielectric constant $\varepsilon(U)$ of the ferroelectric layer on the control voltage. To obtain this dependence, the impedance of the capacitor based on the experimental $\mathrm{Ba_{0.5}Sr_{0.5}TiO_3}$ (BST) sample was measured. To this end, we used an automated digital bridge with the amplitude of the probing signal of 1 V and variable bias voltage $U = 0-400$ V. The capacitance-voltage characteristics were taken at a frequency of 1 MHz. The relative permittivity ε was calculated from the capacitance of the sample measured at the room temperature. The obtained data can be precisely fitted by the following expression:

$$\varepsilon(U) = \frac{\varepsilon(0) - \varepsilon(400)}{1 + (U/U_{00})^2} + \varepsilon(400), \tag{A1}$$

where $\varepsilon(0)$ and $\varepsilon(400)$ are the ferroelectric permittivity for $U = 0$ V and $U = 400$ V, respectively; $U_{00} = \frac{3}{2} S_{\mathrm{eff}} E_{\mathrm{n}} (\frac{\varepsilon_{00}}{\varepsilon(0)})^{3/2}$. Here $E_{\mathrm{n}} = 30$ V/μm and $\varepsilon_{00} = 300$ are the phenomenological parameters that are peculiar to $\mathrm{Ba_{0.5}Sr_{0.5}TiO_3}$ in a paraelectric state at room temperature; S_{eff} is an effective length of the electric field strength line. For the considered case of a sandwich capacitor, this parameter is approximately equal to the ferroelectric thickness ($S_{\mathrm{eff}} \approx \delta$). As a result, the distribution of dielectric permittivity shown in Fig. 3(a) was calculated with the use of the electric field distribution calculated from the Poisson equation taking into account Eq. (A1).

APPENDIX B: DISTRIBUTION OF THE DIELECTRIC PERMITTIVITY ACROSS FERROELECTRICS WITHIN ONE PERIOD OF THE DEMC

In Fig. 3(b), we show the spatial distribution of the dielectric permittivity after application of electrical voltage to the grid electrode within one period of the DEMC. According to the main text, each period was divided into 48 regions with length l_i consisting of two ferrite films and a ferroelectric layer with dielectric permittivity ε_i. Table I gives the values of l_i and ε_i.

APPENDIX C: MODIFIED TRANSFER-MATRIX METHOD

The transmission characteristics of the periodic structure were calculated according to the transfer-matrix method. This method allows one to calculate the transmission characteristics of a finite-length waveguide with rectangular cross sections of the periodic disturbances. Due to a gradually varied dielectric permittivity across the ferroelectric layer in the investigated structure [see Fig. 3(a)], the standard transfer-matrix method was modified to describe the propagation and reflections of waves in the DEMC. To this end, we divided each period of the DEMC into 48 regions with length l_i consisting of two ferrite films and a ferroelectric layer with dielectric permittivity ε_i, where i is any integer from 1 to $P = 48$ [see Fig. 3(b) and Appendix B]. According to the proposed method, matrices $\boldsymbol{T}^{(2i-1)}$ were used to describe the wave propagation in the i region. These

TABLE I. Values of dielectric permittivity ε_i of the ferroelectric layer and its length l_i within one period of the DEMC region.

i	l_i (μm)	ε	i	l_i (μm)	ε
1	6.608	1490	25	10.62	755
2	6.646	1473	26	9.969	759
3	23.15	1410	27	6.646	765
4	6.646	1354	28	9.969	768
5	9.9697	1267	29	6.646	780
6	6.647	1216	30	9.969	789
7	9.9697	1148	31	6.646	804
8	6.6465	1106	32	9.969	819
9	9.9697	1052	33	6.646	843
10	6.6465	1019	34	9.969	858
11	9.9697	974	35	6.646	888
12	6.6465	947	36	9.969	909
13	9.9697	909	37	6.6465	947
14	6.6465	888	38	9.9697	974
15	9.9697	858	39	6.6465	1019
16	6.6465	843	40	9.9697	1052
17	9.9697	819	41	6.6465	1106
18	6.6465	804	42	9.9697	1148
19	9.9697	789	43	6.647	1216
20	6.6465	780	44	9.9697	1267
21	9.9697	768	45	6.6465	1354
22	6.6465	765	46	9.9697	1410
23	9.9697	759	47	6.6465	1473
24	10.621	755	48	6.608	1490

matrices had diagonal components only: $\boldsymbol{T}_{11}^{(2i-1)} = 1/\ \boldsymbol{T}_{22}^{(2i-1)} = \exp[(-jk_{2i} + k_{2i}^{*})l_{2i}]$. Here, k_i and k_i^{*} are real and imaginary parts of a complex wave number of the SEWs propagating in the i region. Matrices $\boldsymbol{T}^{(2i)}$ described reflections of the waves from the edges of neighborhood regions. Considering that the reflection coefficient is $\Gamma = |(k_{2i-1} - k_{2i})/(k_{2i-1} + k_{2i})|$, and the transmission through the junction is $1 - \Gamma$, these matrices are given by $\boldsymbol{T}_{11}^{(2i)} = \boldsymbol{T}_{22}^{(2i)} = 1/(1 - \Gamma)$ and $\boldsymbol{T}_{12}^{(2i)} = \boldsymbol{T}_{21}^{(2i)} = \Gamma/(1 - \Gamma)$. The final transfer-matrix for the multilayered structure formed by $N = 10$ periods was obtained by multiplication of all $\boldsymbol{T}$ matrices: $\boldsymbol{T}_{\Sigma} = (\prod_{i=1}^{2P} \boldsymbol{T}^{(i)})^{N}$. The complex transfer function corresponds to $1/\boldsymbol{T}_{\Sigma 11}$, and the power transmission characteristic of the considered structure is given by $S_{21} = 20\log_{10}(1/|\boldsymbol{T}_{\Sigma 11}|)$. As a result, this approach allows one to calculate the transmission characteristics of the proposed DMC.

APPENDIX D: PRINCIPLE OF THE HYBRID WAVE FORMATION IN FERRITE-FERROELECTRIC THIN FILM MULTILAYERS

In Fig. 4(a), we show the dispersion characteristic of spin-electromagnetic waves in the studied ferrite-ferroelectric thin film multilayers. The presented wave spectrum is determined by two distinct mechanisms of wave interactions. *The first one* is hybridization of the surface spin-wave mode in a ferrite film with the transverse electric (TE_1) mode of the electromagnetic spectrum in a ferroelectric layer. This process leads to formation of the coupled excitations known as hybrid spin-electromagnetic waves (SEWs). The wave hybridization was experimentally observed in artificial multiferroic heterostructures composed of ferrite film and a ferroelectric ceramic slab (see, for example, [52]). The general dipole-exchange theory of SEW spectra in these structures was developed by Demidov *et al.* [28]. The theory predicts that only relatively thick ferroelectric layers (on the order of hundreds of micrometers) provide an effective hybridization of surface spin-wave and TE_1 modes in the GHz frequency range. Such thickness limitation is caused by demands to drop the phase velocity of electromagnetic waves and ensure the intersection of electromagnetic and spin waves at wave numbers $k > 50\,\mathrm{rad/cm}$, where SEWs can be effectively excited in practice. To overcome the ferroelectric thickness limitation, we propose to use the magnetodipole interaction between spin waves in coupled ferrite films. This is *the second mechanism* of wave interactions studied in our work.

Let us describe both mechanisms of wave interactions in ferrite-ferroelectric thin film multilayers by using numerical calculations. To this end, we used the theory developed by Nikitin *et al.* [32], which was also applied for theoretical modeling of the thin film electromagnonic crystal. During the modeling, we used the same set of parameters as in the main text. Namely, the ferroelectric layer had a thickness of $\delta = 25\,\mu\mathrm{m}$ and zero voltage permittivity of $\varepsilon(0) = 1490$, the top ferrite film had a thickness of $t_1 = 13.6\,\mu\mathrm{m}$ and saturation magnetization of $M_1 = 143.24$ kA/m, and the bottom ferrite layers had a thickness of $t_2 = 5.5\,\mu\mathrm{m}$ and saturation magnetization of $M_2 = 153.58$ kA/m. The results of the modeling are shown in Fig. 7 demonstrating the features of the hybrid wave formation in the ferrite-ferroelectric thin film multilayers.

The dispersion characteristics presented in Fig. 7 can be described as follows. If the distance between the ferrite and ferroelectric films is much greater than operating wavelengths λ [see Fig. 7(a)], then the electromagnetic and spin waves do not interact with each other. In the ferrite-ferroelectric bilayer, these waves are hybridized as shown in Fig. 7(b). The physical reason behind this behavior is caused by *the first mechanism* of the wave interaction. In contrast to thick ferroelectric slabs, the electromagnetic wave in thin film structures demonstrates a fast-growing phase velocity with frequency. It means that electromagnetic and spin waves have similar phase velocities at low wave numbers k only. As follows from the inset of Fig. 7(b), this area of effective coupling between modes is realized for $k < 10$ rad/cm. For higher k, the SEW dispersion curve tends to the pure spin-wave branch that is shown in Fig. 7(b). Therefore, an electric tuning by varying the ferroelectric layer permittivity will be inefficient in the region where the SEW can be effectively excited in practice.

The second mechanism of the wave interaction is examined in Figs. 7(c) and 7(d). Figure 7(c) shows the calculated dispersion characteristics of uncoupled spin waves propagating in two nonidentical ferrite films. As follows from Sec. II, the thickness and saturation magnetization of these layers were chosen to provide an intersection of the dispersion characteristics. According to coupled mode theory [53], the strength of an interaction between modes depends on a phase mismatch. The considered set of parameters yields a wide

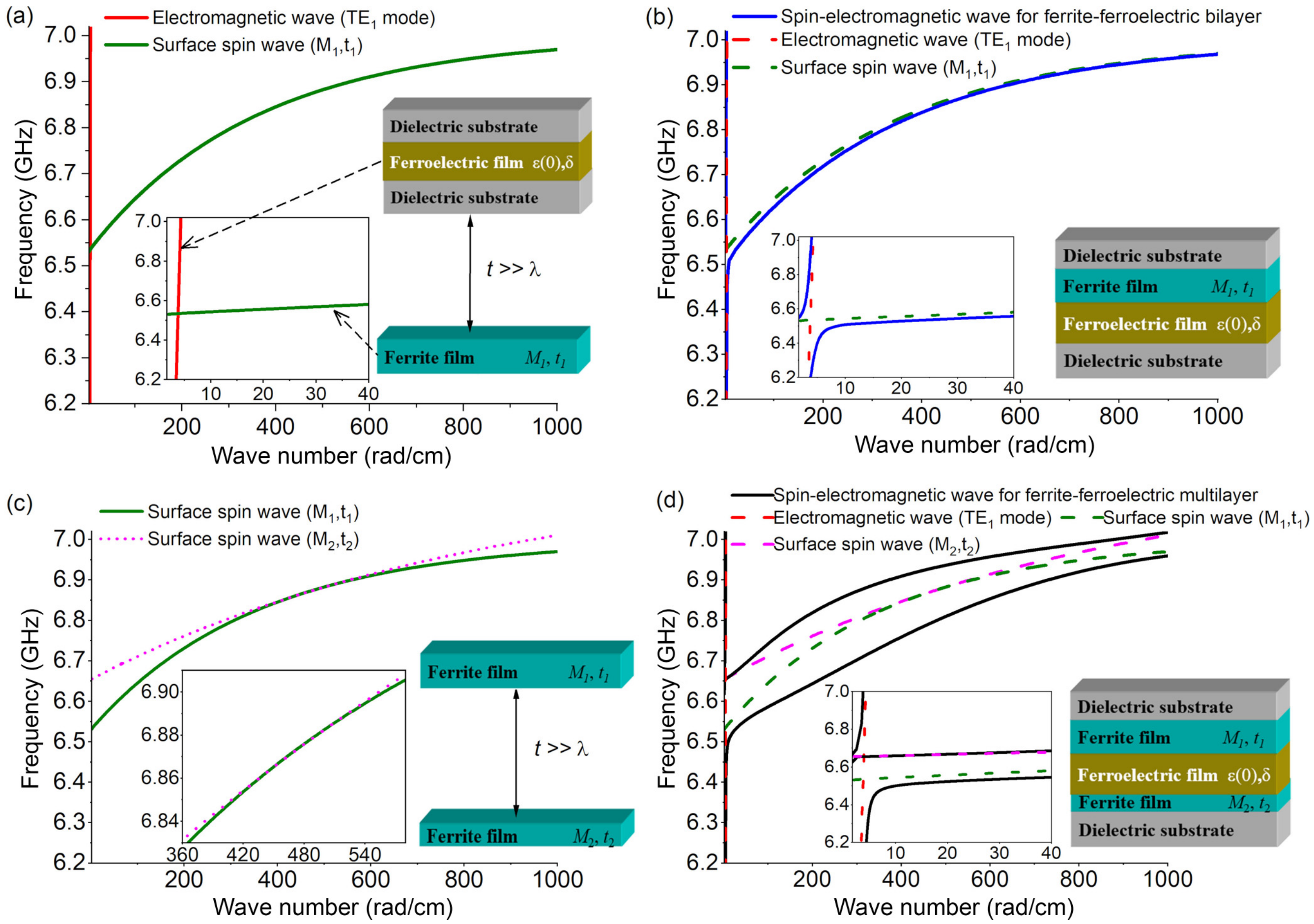

FIG. 7. Dispersion characteristics of (a) the TE$_1$ mode (solid red line) in the ferroelectric film and surface spin wave (solid green line) in the ferrite film; (b) the spin-electromagnetic wave (solid blue lines) propagating in the ferrite-ferroelectric bilayer; (c) the surface spin waves in the uncoupled ferrite films; (d) the spin-electromagnetic wave (solid black lines) propagating in the ferrite-ferroelectric multilayer. In this figure, the insets demonstrate a schematic view of the studied structures. In insets (a,c), t is a thickness of the nonmagnetic spacer layer, which is much greater than operating wavelengths λ. Additional insets show fragments of the dispersion characteristics, where the intersection of the dispersion characteristics is realized in the expanded scale. For the sake of comparison, (b,d) also present dispersion curves of TE$_1$ mode (dashed red line), surface spin waves in thick (dashed green line), and thin (dashed magenta line) ferrite films.

range of wave numbers from 360 to 580 rad/cm where the phase velocities of the waves in uncoupled ferrite films are close [see inset of Fig. 7(c)]. As the distance between the ferrite films t is decreased, the spin waves start to interact which manifests itself in a repulsion of their dispersion characteristics. As seen in Fig. 7(d), the small distance between the ferrites (equal to ferroelectric thickness $t = \delta = 25\,\mu\text{m}$) leads to a strong repulsion of the SEW dispersion branches in a wide range of wave numbers from 100 to 900 rad/cm. This effect paves the way to effective electric field control of wave dynamics in ferrite-ferroelectric thin film multilayers.

To estimate a range of electric field tuning, we performed additional numerical calculations presented in Fig. 8. As is well known, the application of an electric field to a ferroelectric layer decreases its relative dielectric permittivity ε resulting in an increase of phase velocity of electromagnetic waves. This means that a decrease in ε shifts the regions of wave hybridization towards the ordinate axis and decreases the wave numbers of the SEW for fixed frequencies. This behavior is clearly visible in Fig. 8(a), where dispersion characteristics in the ferrite-ferroelectric bilayer were calculated for two values of the dielectric permittivity $\varepsilon(0\,\text{V}) = 1490$ and $\varepsilon(120\,\text{V}) = 755$. However, the region of effective electric tuning of the SEW dispersion characteristics is located at low wave numbers k only because of the thin ferroelectric layer thickness. As a result, this region is out of wave numbers, where rejection bands can be formed for electromagnonic crystals based on a thin ferroelectric layer. To demonstrate this, we added vertical dash-dotted lines corresponding to Bragg wave vector $k_B = n\pi/\Lambda$, where n is a band-gap number, and Λ is 400 μm. As seen from Fig. 8(a), a frequency shift Δf of the dispersion characteristic is equal to 3 MHz at a fixed wave number of a first rejection band. This value is not enough to see a pronounced rejection band in the experiment.

Consider now the influence of the same variation of ε on dispersion characteristics of SEWs in two ferrite films separated by a thin ferroelectric layer as shown in Fig. 8(b). As in the previous case, an effective electric tuning of the SEW dispersion characteristic is realized near the region of

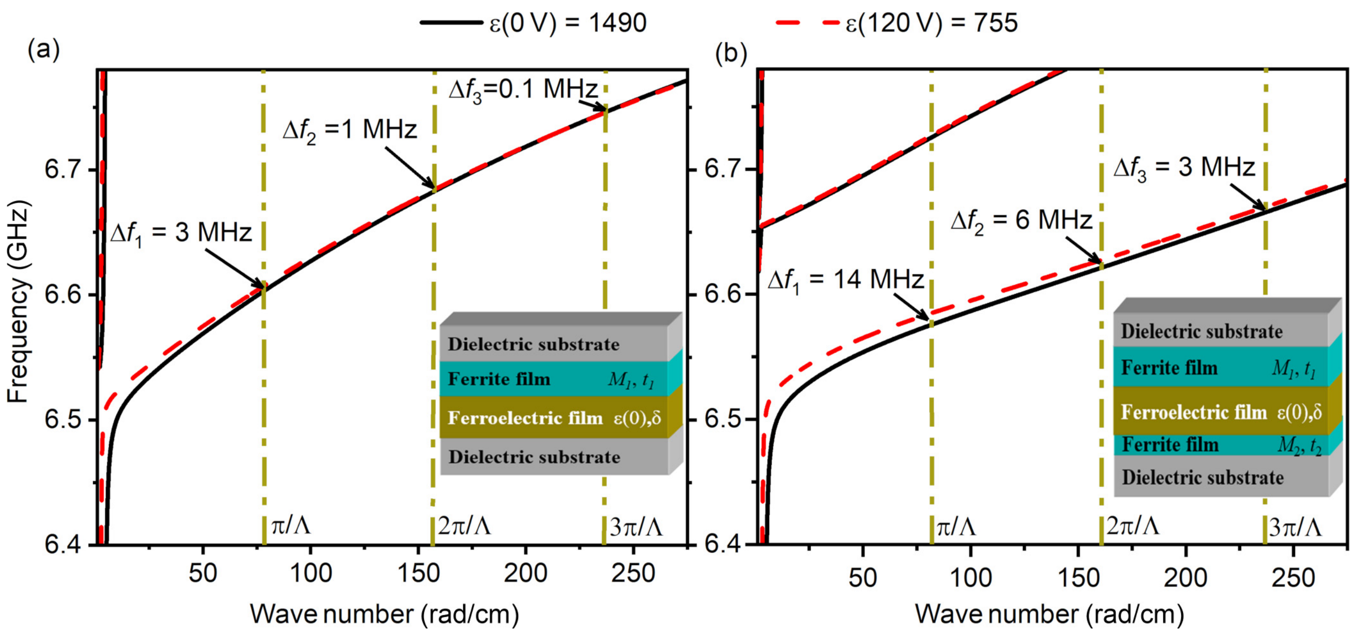

FIG. 8. (a) Dispersion characteristics of the SEWs in the ferrite-ferroelectric bilayer calculated for dielectric permittivity $\varepsilon(0\,\text{V}) = 1490$ (black solid line) and $\varepsilon(120\,\text{V}) = 755$. (b) Dispersion characteristics of the SEWs in the ferrite-ferroelectric-ferrite thin film structure calculated for dielectric permittivity $\varepsilon(0\,\text{V}) = 1490$ (black solid line) and $\varepsilon(120\,\text{V}) = 755$. Dash-dotted vertical lines show the frequencies that correspond to the wave numbers satisfying the Bragg reflection for the design shown in Fig. 1 of the main text.

strong coupling between TE_1 and spin-wave modes. However, a detailed study also shows changes in the spectrum far from this region. Namely, for $k > 50\,\text{rad/cm}$, a variation of ε leads to a shift of the dispersion branches because of a change in the coupling strength between spin-wave modes. As a result, the frequency shift Δf of 14 MHz is achieved for the studied multilayers at a fixed wave number of a first rejection band. This feature allows one to observe a pronounced rejection band in the wave spectrum of the electromagnonic crystal as shown in Fig. 4 of the main text.

[1] P. Pirro, V. I. Vasyuchka, A. A. Serga, and B. Hillebrands, Advances in coherent magnonics, Nat. Rev. Mater. **6**, 1114 (2021).

[2] A. Barman, G. Gubbiotti, S. Ladak, A. O. Adeyeye, M. Krawczyk, J. Gräfe, C. Adelmann, S. Cotofana, A. Naeemi, V. I. Vasyuchka *et al.*, The 2021 magnonics roadmap, J. Phys.: Condens. Matter **33**, 413001 (2021).

[3] A. V. Chumak, P. Kabos, M. Wu, C. Abert, C. Adelmann, A. Adeyeye, J. Åkerman, F. G. Aliev, A. Anane, A. Awad *et al.*, Advances in magnetics roadmap on spin-wave computing, IEEE Trans. Magn. **58**, 1 (2022).

[4] J. D. Costa, B. Figeys, X. Sun, N. Van Hoovels, H. A. Tilmans, F. Ciubotaru, and C. Adelmann, Compact tunable YIG-based rf resonators, Appl. Phys. Lett. **118**, 162406 (2021).

[5] Z. Li, X. Zhang, D. Zhang, B. Liu, H. Meng, J. Xu, Z. Zhong, X. Tang, H. Zhang, and L. Jin, Magnetization dynamics in the YIG/Au/YIG magnon valve, APL Mater. **10**, 021101 (2022).

[6] A. Talapatra, H. Qin, F. Schulz, L. Yao, L. Flajšman, M. Weigand, S. Wintz, and S. van Dijken, Imaging of short-wavelength spin waves in a nanometer-thick YIG/Co bilayer, Appl. Phys. Lett. **122**, 202404 (2023).

[7] A. A. Nikitin, A. A. Nikitin, A. B. Ustinov, S. Watt, and M. P. Kostylev, Theoretical model for nonlinear spin-wave transient processes in active-ring oscillators with variable gain and its application for magnonic reservoir computing, J. Appl. Phys. **131**, 113903 (2022).

[8] S. R. Lake, B. Divinskiy, G. Schmidt, S. O. Demokritov, and V. E. Demidov, Microscopic nonlinear magnonic phase shifters based on ultrathin films of a magnetic insulator, Appl. Phys. Lett. **121**, 052403 (2022).

[9] V. V. Vitko, A. A. Nikitin, R. V. Haponchyk, A. A. Stashkevich, M. P. Kostylev, and A. B. Ustinov, Bistable behavior of active ring resonator on surface spin waves, Eur. Phys. J. Plus **137**, 1010 (2022).

[10] A. B. Ustinov, A. V. Drozdovskii, and B. A. Kalinikos, Multifunctional nonlinear magnonic devices for microwave signal processing, Appl. Phys. Lett. **96**, 142513 (2010).

[11] A. V. Chumak, A. A. Serga, and B. Hillebrands, Magnon transistor for all-magnon data processing, Nat. Commun. **5**, 1 (2014).

[12] S. Atalay, A. O. Kaya, V. S. Kolat, H. Gencer, and T. Izgi, One-dimensional magnonic crystal for magnetic field sensing, J. Supercond. Novel Magn. **28**, 2071 (2015).

[13] P. J. Metaxas, M. Sushruth, R. A. Begley, J. Ding, R. C. Woodward, I. S. Maksymov, M. Albert, W. Wang, H. Fangohr, A. O. Adeyeye, and M. Kostylev, Sensing magnetic nanoparticles using nano-confined ferromagnetic resonances in a magnonic crystal, Appl. Phys. Lett. **106**, 232406 (2015).

[14] E. Bankowski, T. Meitzler, R. S. Khymyn, V. S. Tiberkevich, A. N. Slavin, and H. X. Tang, Magnonic crystal as a delay line for low-noise auto-oscillators, Appl. Phys. Lett. **107**, 122409 (2015).

[15] A. A. Nikitin, A. A. Nikitin, A. B. Ustinov, A. E. Komlev, E. Lähderanta, and B. A. Kalinikos, Metal-insulator switching of vanadium dioxide for controlling spin-wave dynamics in magnonic crystals, J. Appl. Phys. **128**, 183902 (2020).

[16] H. Merbouche, M. Collet, M. Evelt, V. E. Demidov, J. Prieto, M. Muñoz, J. Ben Youssef, G. de Loubens, O. Klein, S. Xavier *et al.*, Frequency filtering with a magnonic crystal based on nanometer-thick yttrium iron garnet films, ACS Appl. Nano Mater. **4**, 121 (2021).

[17] R. V. Haponchyk and A. B. Ustinov, Nonlinear phase shifts induced by pumping spin waves in magnonic crystals, Appl. Phys. Lett. **122**, 212401 (2023).

[18] A. V. Chumak, V. S. Tiberkevich, A. D. Karenowska, A. A. Serga, J. F. Gregg, A. N. Slavin, and B. Hillebrands, All-linear time reversal by a dynamic artificial crystal, Nat. Commun. **1**, 141 (2010).

[19] M. Vogel, A. V. Chumak, E. H. Waller, T. Langner, V. I. Vasyuchka, B. Hillebrands, and G. Von Freymann, Optically reconfigurable magnetic materials, Nat. Phys. **11**, 487 (2015).

[20] A. A. Nikitin, A. B. Ustinov, A. A. Semenov, A. V. Chumak, A. A. Serga, V. I. Vasyuchka, E. Lähderanta, B. A. Kalinikos, and B. Hillebrands, A spin-wave logic gate based on a width-modulated dynamic magnonic crystal, Appl. Phys. Lett. **106**, 102405 (2015).

[21] R. G. Kryshtal and A. V. Medved, Surface acoustic waves in dynamic magnonic crystals for microwave signals processing, Ultrasonics **94**, 60 (2019).

[22] A. A. Nikitin, A. E. Komlev, A. A. Nikitin, A. B. Ustinov, and E. Lähderanta, Dynamic magnonic crystals based on vanadium dioxide gratings, Phys. Rev. Appl. **20**, 044026 (2023).

[23] Q. Wang, A. V. Chumak, L. Jin, H. Zhang, B. Hillebrands, and Z. Zhong, Voltage-controlled nanoscale reconfigurable magnonic crystal, Phys. Rev. B **95**, 134433 (2017).

[24] G. Sietsema, T. Liu, and M. E. Flatté, Electric-field control of magnon gaps in a ferromagnet using a spatially-periodic electric field, Spin **7**, 1740012 (2017).

[25] B. Rana and Y. Otani, Voltage-controlled reconfigurable spin-wave nanochannels and logic devices, Phys. Rev. Appl. **9**, 014033 (2018).

[26] H. Merbouche, I. Boventer, V. Haspot, S. Fusil, V. Garcia, D. Gouéré, C. Carrétéro, A. Vecchiola, R. Lebrun, P. Bortolotti *et al.*, Voltage-controlled reconfigurable magnonic crystal at the sub-micrometer scale, ACS Nano **15**, 9775 (2021).

[27] B. Divinskiy, H. Merbouche, V. E. Demidov, K. O. Nikolaev, L. Soumah, D. Gouéré, R. Lebrun, V. Cros, J. Ben Youssef, P. Bortolotti *et al.*, Evidence for spin current driven Bose-Einstein condensation of magnons, Nat. Commun. **12**, 1 (2021).

[28] V. E. Demidov, B. A. Kalinikos, and P. Edenhofer, Dipole-exchange theory of hybrid electromagnetic-spin waves in layered film structures, J. Appl. Phys. **91**, 10007 (2002).

[29] A. B. Ustinov and B. A. Kalinikos, Multiferroic periodic structures based on magnonic crystals for electronically tunable microwave devices, Tech. Phys. Lett. **40**, 568 (2014).

[30] M. A. Morozova, O. V. Matveev, A. M. Markeev, A. G. Chernikova, A. M. Mednikov, S. A. Gusev, I. Y. Pashenkin, N. S. Gusev, D. V. Romanenko, and S. A. Nikitov, Magnetoelectric hysteresis of Bragg resonances in a multiferroic crystal based on YIG/HZO, Phys. Rev. B **108**, 174407 (2023).

[31] A. B. Ustinov, A. V. Drozdovskii, A. A. Nikitin, A. A. Semenov, D. A. Bozhko, A. A. Serga, B. Hillebrands, E. Lähderanta, and B. A. Kalinikos, Dynamic electromagnonic crystal based on artificial multiferroic heterostructure, Commun. Phys. **2**, 137 (2019).

[32] A. A. Nikitin, A. B. Ustinov, V. V. Vitko, A. A. Nikitin, A. V. Kondrahov, P. Pirro, E. Lähderanta, B. A. Kalinikos, and B. Hillebrands, Spin-electromagnetic waves in planar multiferroic multilayers, J. Appl. Phys. **122**, 014102 (2015).

[33] A. A. Nikitin, A. A. Nikitin, A. V. Kondrashov, A. B. Ustinov, B. A. Kalinikos, and E. Lähderanta, Theory of dual-tunable thin-film multiferroic magnonic crystal, J. Appl. Phys. **122**, 153903 (2017).

[34] B. Peng, H. Tang, Y. Cheng, Y. Zhang, R. Qiu, Q. Lu, Z. Zhou, and M. Liu, Voltage control of perpendicular magnetic anisotropy in multiferroic composite thin films under strong electric fields, ACS Appl. Mater. Interfaces **13**, 61404 (2021).

[35] A. A. Nikitin, V. V. Vitko, A. A. Nikitin, A. V. Kondrashov, A. B. Ustinov, A. A. Semenov, and E. Lähderanta, Dual tuning of doubly hybridized spin-electromagnetic waves in all-thin-film multiferroic multilayers, IEEE Trans. Magn. **53**, 1 (2017).

[36] M. A. Morozova, D. V. Romanenko, O. V. Matveev, S. V. Grishin, Y. P. Sharaevskii, and S. A. Nikitov, Suppression of periodic spatial power transfer in a layered structure based on ferromagnetic films, J. Magn. Magn. Mater. **466**, 119 (2018).

[37] A. A. Nikitin, A. A. Nikitin, A. B. Ustinov, E. Lähderanta, and B. A. Kalinikos, Theory of spin-electromagnetic waves in planar thin-film multiferroic heterostructures based on a coplanar transmission line and its application for electromagnonic crystals, IEEE Trans. Magn. **54**, 1 (2018).

[38] P. Graczyk, M. Zelent, and M. Krawczyk, Co-and contra-directional vertical coupling between ferromagnetic layers with grating for short-wavelength spin wave generation, New J. Phys. **20**, 053021 (2018).

[39] A. A. Nikitin, V. V. Vitko, A. A. Nikitin, A. B. Ustinov, and B. A. Kalinikos, Miniature multiferroic interferometer for voltage-controlled spin-wave logic gates, in *Proceedings of the Photonics & Electromagnetics Research Symposium–Spring* (IEEE, New York, 2019), pp. 1547–1551.

[40] A. A. Nikitin, A. A. Nikitin, I. L. Mylnikov, A. B. Ustinov, and B. A. Kalinikos, Electromagnonic crystals based on ferrite–ferroelectric–ferrite multilayers, IET Microwave Antennas Propag. **14**, 1304 (2020).

[41] K. Mori, T. Goto, T. Watanabe, T. Koguchi, Y. Nakamura, P. B. Lim, A. B. Ustinov, and M. Inoue, Broadband excitation of spin wave using microstrip line antennas for integrated magnonic devices, J. Phys. D **55**, 115002 (2021).

[42] A. V. Chumak, A. A. Serga, B. Hillebrands, and M. P. Kostylev, Scattering of backward spin waves in a one-dimensional magnonic crystal, Appl. Phys. Lett. **93**, 022508 (2008).

[43] Y. Zhu, K. H. Chi, and C. S. Tsai, Magnonic crystals-based tunable microwave phase shifters, Appl. Phys. Lett. **105**, 022411 (2014).

[44] P. Frey, A. A. Nikitin, D. A. Bozhko, S. A. Bunyaev, G. N. Kakazei, A. B. Ustinov, B. A. Kalinikos, F. Ciubotaru, A. V. Chumak, Q. Wang, V. S. Tiberkevich, B. Hillebrands, and A. A. Serga, Reflection-less width-modulated magnonic crystal, Commun. Phys. **3**, 1 (2020).

[45] F. Ciubotaru, A. V. Chumak, B. Obry, A. A. Serga, and B. Hillebrands, Magnonic band gaps in waveguides with a periodic variation of the saturation magnetization, Phys. Rev. B **88**, 134406 (2013).

[46] H. Qin, G. J. Both, S. J. Hämäläinen, L. Yao, and S. van Dijken, Low-loss YIG-based magnonic crystals with large tunable bandgaps, Nat. Commun. **9**, 5445 (2018).

[47] N. Kanazawa, T. Goto, J. W. Hoong, A. Buyandalai, H. Takagi, and M. Inoue, Metal thickness dependence on spin wave propagation in magnonic crystal using yttrium iron garnet, J. Appl. Phys. **117**, 17E510 (2015).

[48] P. Grünberg, Magnetostatic spinwave modes of a ferromagnetic double layer, J. Appl. Phys. **51**, 4338 (1980).

[49] G. Carlotti and G. Gubbiotti, Brillouin scattering and magnetic excitations in layered structures, Riv. Nuovo Cimento **22**, 1 (1999).

[50] J. F. Cochran, Brillouin light scattering from periodic multilayers composed of very thin magnetic films, Phys. Rev. B **64**, 134406 (2001).

[51] G. Gubbiotti, S. Tacchi, H. T. Nguyen, M. Madami, G. Carlotti, K. Nakano, T. Ono, and M. G. Cottam, Coupled spin waves in trilayer films and nanostripes of permalloy separated by nonmagnetic spacers: Brillouin light scattering and theory, Phys. Rev. B **87**, 094406 (2013).

[52] A. B. Ustinov, G. Srinivasan, and B. A. Kalinikos, Ferrite-ferroelectric hybrid wave phase shifters, Appl. Phys. Lett. **90**, 031913 (2007).

[53] A. A. Barybin and V. A. Dmitriev, *Modern Electrodynamics and Coupled-Mode Theory: Application to Guided-Wave Optics* (Rinton Press, Princeton, NJ, 2002), Part I.